# PART II

# EXPERIMENTAL DESCRIPTION

# PART II – EXPERIMENTAL DESCRIPTION

In this part there is a detailed description of the deposition sets used for the preparation of DLC structures. It is of capital importance not only choosing the most adequate deposition method, but also designing properly the reactor and providing it a complete data acquisition system for an accurate process control.

The DLC samples were deposited by using low-pressure plasma techniques in two different vacuum chambers, as described in chapter 3. Amorphous hydrogenated carbon (a-C:H or DLC) films were prepared by pulsed-DC PECVD using only methane as precursor. All the processes were carried out at room temperature, because, as explained in introductory chapter 2, film growth on cold substrates favours the amorphous state. DLC films with uniform metal content (Me-DLC) were deposited in another reactor by pulsed-DC reactive magnetron sputtering of metallic targets in an atmosphere with argon and methane. By modifying the vessel configuration it was possible to deposit multilayer structures of carbon/metal/…/metal (Me/a-C). A list containing the deposited samples in this study can be found in appendix A.

In-situ characterization of the glow discharge responsible of DLC growth by PECVD was performed through a computer controlled fast Langmuir probe, which recorded I(V) characteristics with a high time resolution. For this purpose, a time-delay circuit was constructed in order to diminish the frequency of the power supply trigger and therefore register synchronously the plasma parameters. Gas pressure was red by manometers, and set by both gas flow variation and quenching of the vacuum line through a manual valve. The time evolution of cathode voltage was monitored by an oscilloscope.

The technology employed for the ulterior characterization of the samples is listed in chapter 4. The morphological and structural study was carried out mainly by TEM, XRD and AFM. Composition was studied by XPS and EPMA. Mechanical and tribological properties were obtained by nanoindentation, scratch and Calo-wear tests, and new accessories based in AFM for nano-tribology measurements and based in SPM for surface conductivity scanning were also developed.

# Chapter 3

# Experimental set for deposition

# Chapter 3 – Experimental set for deposition

## 3.1. Experimental set for deposition of amorphous carbon by pulsed-DC plasma enhanced CVD (PECVD)

The deposition system consisted in a plasma reactor with a load-lock chamber and a computer controlled gas supply and pumping system. Figure 3.1 shows a schematic of this reactor. The deposition chamber was a cylindrical stainless-steel vacuum vessel of 30 cm diameter, with two faced planar electrodes of 70 and 400 $cm^2$ in area, which are placed vertically 4 cm away. They worked as cathode and as grounded electrode, respectively. This configuration should be reproduced if preparation of additional samples with comparable properties is required, because the relationship between bias voltage and supplied power for a given system depends on the electrode geometry [Liebermann M.A., 2005].

The substrates were placed onto the PECVD cathode, which was maintained at room temperature during all the processes by using a cool-water circuit. Figure 3.6 in section 3.2 shows a cross-section of a sputtering header, whose architecture was similar to that of PECVD cathode. Because of the vertical surface of substrate electrode, the substrates were fixed by using Loctite glue.

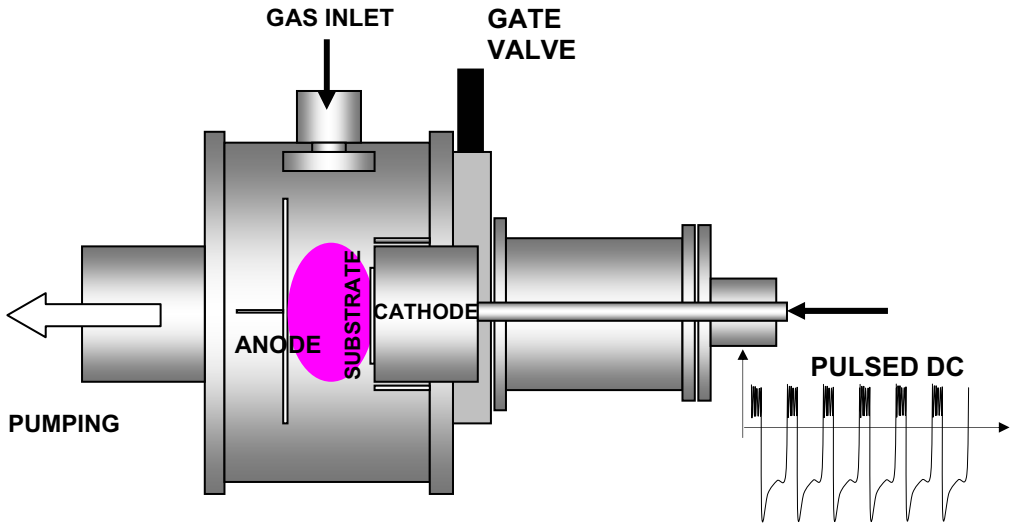


Figure 3.1: Schematic diagram of the pulsed-DC PECVD system.

The $CH_4$ gas was introduced into the reactor at flow rate of 30 sccm as measured by a mass flow controller (MFC). Through LabView software we controlled the valves installed in the gas line system. The gas flowed downstream along the interelectrode gap and was evacuated with a Roots pump coupled to a mechanical pump during the deposition process. Prior to each process, the chamber was evacuated by a turbomolecular pump up to achieve a base pressure of $3 \cdot 10^{-4}$ Pa. It is a very important step to minimise contamination of the samples. The deposition pressure was 10 Pa, as measured by a capacitance manometer. Thus, contaminating gases contribute less than 1% to the total pressure. Figure 3.2 shows a scheme of the gas and evacuation lines of the PECVD chamber.

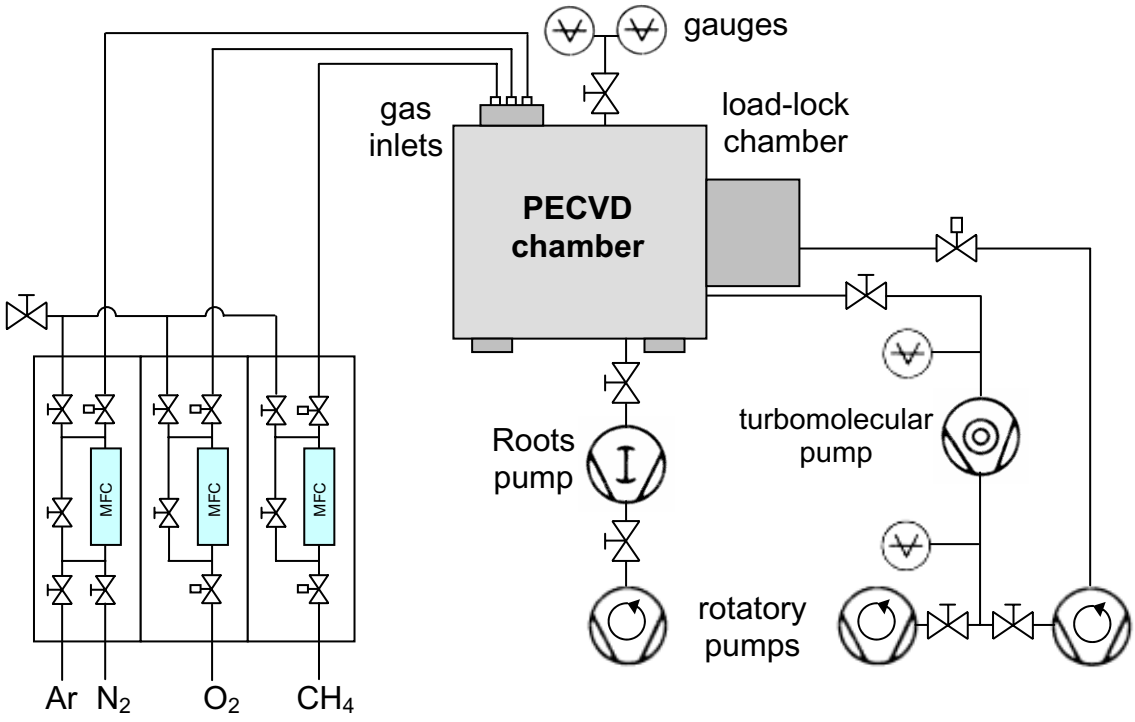


Figure 3.2: Scheme of the gas and evacuation lines of the PECVD reaction chamber.

RF and pulsed-DC supplies powered the substrate electrode. A programmable RF source biased it from -200 up to -800 V. On the other hand, an asymmetrical bipolar pulsed-DC voltage waveform was supplied by an ENI RPG-50 source (50-250 kHz), which operated in power regulation mode. Peak voltages varied between -600 and -1400 V. Figure 3.3 defines the basic structure of a voltage signal associated to pulsed power.

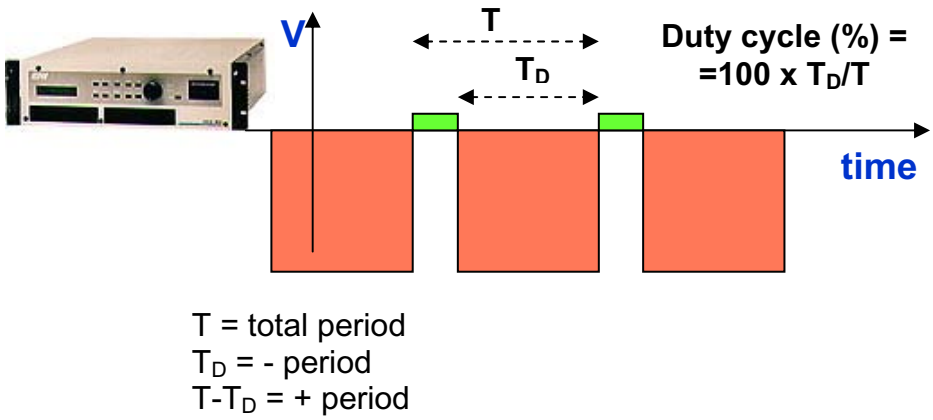


Figure 3.3: Voltage signal supplied by the pulsed power source.

A pulse cycle shows two regions. $T_-$ and $T_+$ periods correspond to the negative (energetic) and positive (non-energetic) signals, respectively. This introduces the bipolar character to the voltage. This pulsed-DC discharge is also called asymmetric because, aside of being weaker, reversal period ($T_+$) is shorter than the negative one. This reversal signal is a constant of 40 V, and supposes a mechanism to avoid arcing due to charge release. Figure 3.4 shows a sketch of a pulsed voltage signal in more detail.

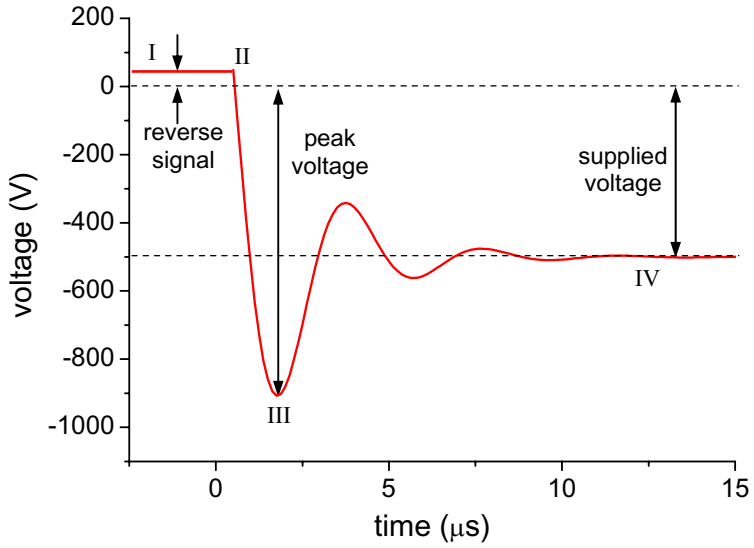


Figure 3.4: Definition of parameters in a pulsed voltage signal.

Four regions are distinguished within the pulsed signal. The region I is a default positive voltage (40 V) set by fabricant to avoid arcing. A sudden decrease of voltage is detected in point II. From there, the driven signal reaches a minimum that is the *peak voltage*

(point III). Following this point, the voltage oscillates by reducing amplitude and tending to a limit value. This steady voltage is the *supplied voltage*, and defines the region IV.

The achievement of high voltages at the point III in figure 3.4 constitutes one of the main advantages of depositing DLC films by pulsed-DC technology. One can obtain punctually large energies in the ion flow (> 1000 eV) in the glow discharge by supplying moderate values of power (~ 100 W). Furthermore, the operation of a pulsed-DC generator does not need the installation of a matching box, reducing the production cost of DLC films with respect to RF-deposition. Thus, this technique presents many advantages that make it appropriated to prepare good-quality DLC coatings.

Pulse frequencies were selected between 100 and 200 kHz. This election is based on the electric resistivity of the deposited film. In fact, reciprocal of charge-up times for insulators in a glow discharge is the corresponding frequency needed to maintain a stable sputtering or deposition process [Chapman B., 1980]. This frequency is about 1 kHz in DLC; therefore stable processes are expected at higher frequencies.

The deposition control parameters were the peak voltage amplitude and the pulse frequency of the signal. Both were visualized on an oscilloscope screen. A study of the plasma parameters along a wavelength period was performed by a Langmuir probe, whose operation is explained in section 3.3.

## 3.2. Experimental set for deposition of metal containing DLC

For metal containing DLC films deposition we must distinguish between two sample structures: DLC films with metal incorporation (Me-DLC), and Me/a-C multilayers. In both we have utilised the same reactor, although the deposition techniques are different and, thus, the experimental set was properly conditioned.

### 3.2.1. DLC with metal incorporation

Me-DLC films were deposited by reactive magnetron sputtering in a cylindrical vessel containing two faced cathodes. One of them contained a magnetron and supported a metal target, and the other one worked as substrate-holder. Figure 3.5 shows a schematic of the reactor chamber. Such configuration was appropriate to achieve a stationary incorporation rate for metal atoms and gas precursor species during all deposition process.

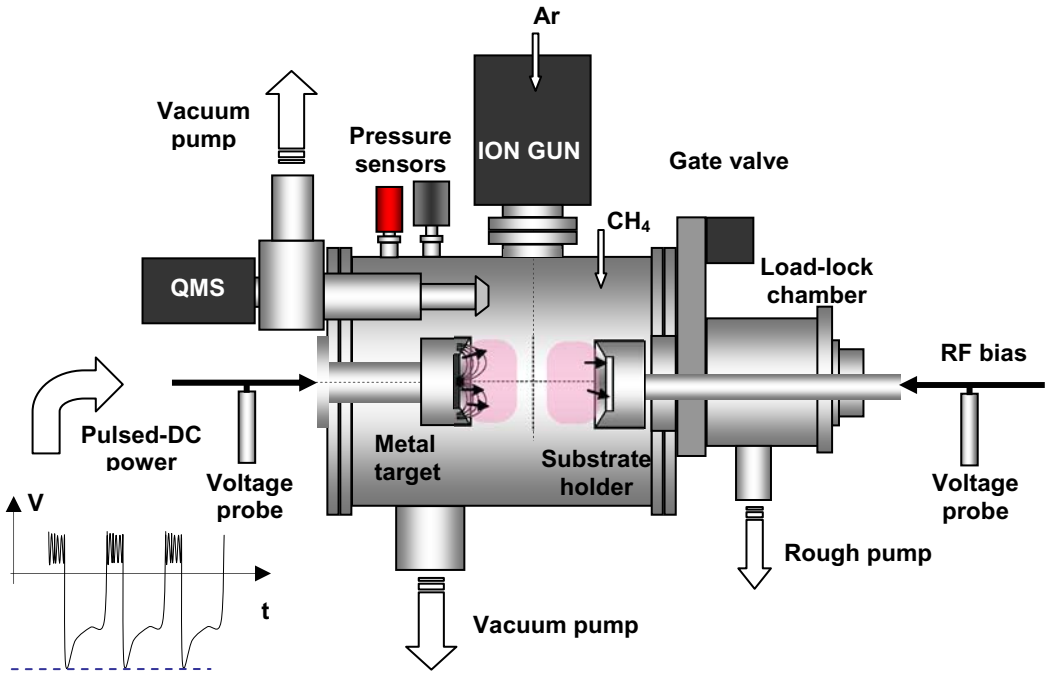


Figure 3.5: Layout of deposition set for Me-DLC films preparation by pulsed-DC reactive magnetron sputtering.

Supporting surfaces of the cathodes were vertically oriented, so fixing materials for targets and substrates were required. The metal targets were pressed onto cathode surface by a round O-ring. Target cooling was efficient due to the good heat conductivity of metals. The

substrates were fixed by Kapton, which consisted in a sticking polyimide film with a low-degassing rate and resistive to a wide temperature range (from -269 to 400ºC). This configuration also minimised the dust incorporation from plasma on the growing films, since formed dust would fall onto the lower part of the vessel.

Both sputtering and substrate electrodes were connected to their respective power suppliers. Every one acted as a cathodic sputtering gun. Hence, they generated different plasmas as shows figure 3.5. The sputtering cathode was powered by a pulsed-DC supplier operated in power regulation mode, whereas an RF power supply fed the substrate cathode. Similar to the use of RF, insulating films have been successfully deposited by bipolar pulsed-DC plasma sputtering in previous works [Sellers J., 1998] [Scholl R.A., 1998].

These cathodes were specially designed to lodge two separated circuits of water flow and electric signals. Figure 3.6 shows a cross section of the designed sputtering header.

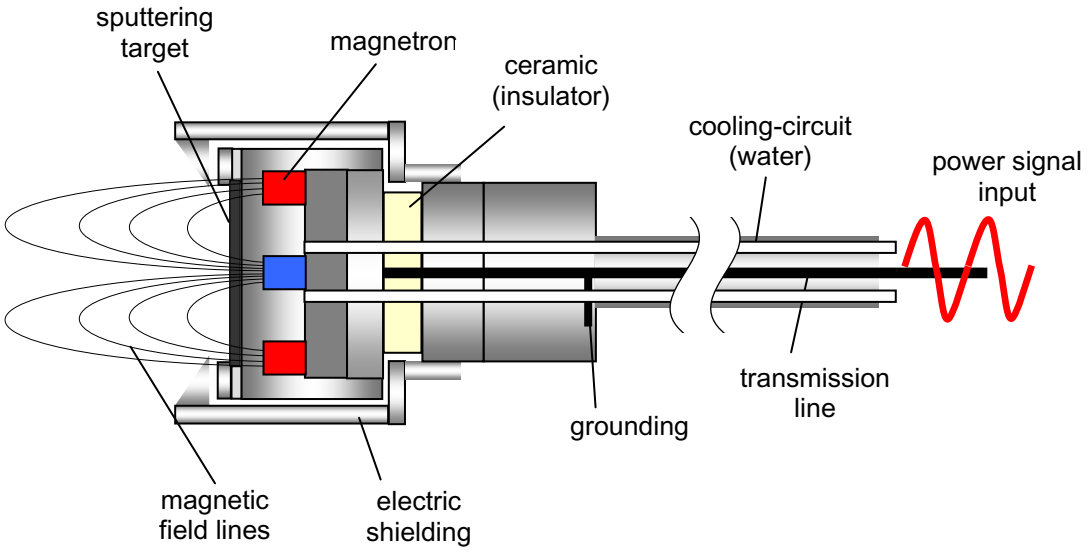


Figure 3.6: Cross-section of the sputtering header equipped with a magnetron, which was used for the deposition of Me-DLC thin films. The design of the substrate-holder is identical, but it does not contain a magnetron and substrates are used instead of targets.

Cooling of the cathodes was supplied by a cool-water circuit. Such cooling was required in the operation of the sputtering gun to protect the magnetron from heating. Indeed, high temperatures damage the magnetron by loosing its magnetisation. Ferromagnetic materials become irreversibly paramagnetic when Curie's temperature is achieved, which can be

avoided through this extra-cooling. Substrate-holder was also cooled in order to impose a film growth far from equilibrium and, hence, deposit amorphous samples.

3-inch diameter sputtering targets of Mo, Nb, Ti and W of 99.99% purity have been employed. These materials were selected because of their trend to form metal carbide nanoparticles within the film network. In fact, Me-DLC films that lodge ceramic inclusions (MoC, TiC) exhibit higher hardness than in non-carbidic compounds (DLC with Au, Al) [Zhang P., 2002]. In the latter case, the influence of the used metal on mechanical performance is still not well known.

This reactor was equipped with two load-lock chambers, so the introduction and removing of substrates and sputtering targets were feasible without breaking the vacuum in the vessel. The other cathode header, left side on figure 3.5, was kept installed. Thus, it could not be removed unless the rector was opened.

Precursor gases were introduced into the chamber through a computer controlled gas line. The pipes coming from gas bottles were connected to an array of MFC, everyone with an alternative by-pass aside. These instruments are regulators of the gas flow. Since MFC were calibrated with Ar and $CH_4$, the introduction of a correction factor was not necessary for flow data reading. The valves located up and down of every MFC were managed by means of a LabView virtual panel.

A Leybold turbo-molecular pump was employed to reach a high vacuum inside the vessel. One of two possible backing pumps could be selected, as a function of the employed gas. This possibility was considered for security reasons. Although only argon and methane were used to deposit DLC structures, this reactor was also destined to obtain other materials, as for instance metal oxides and doped DLC. Eventually, it permitted to perform surface ion treatments. In order to avoid the mixing of reactive gases, a mechanical pump was specifically used for argon and oxygen pumping, and the other one only for methane. A scheme of the sputtering chamber is shown in figure 3.7.

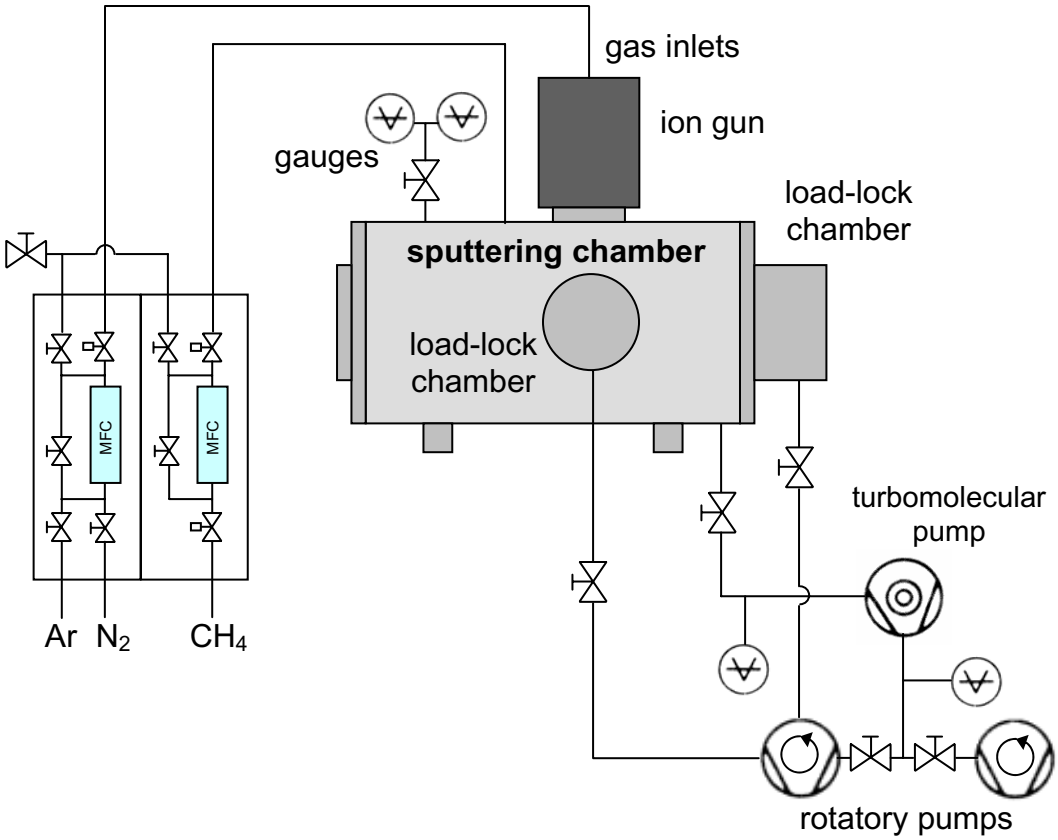


Figure 3.7: Scheme of the sputtering chamber and the gas lines and pumping system..

### 3.2.2. Metal / a-C multilayers

Our objective consists in depositing multilayer films containing alternated DLC and metal layers. The control parameter is the *wavelength* or periodicity of the multilayer, defined as the thickness of a bilayer Me/C, and located in the nanometric scale. For this purpose, we have employed the same deposition set described in 3.2.1. However, the cathodes located on every side were prepared as magnetron sputtering headers. The substrates were placed onto a rotatory holder incorporated between both sputtering targets. By switching the orientation of this holder we selected the acting target and, therefore, the depositing material (figure 3.8).

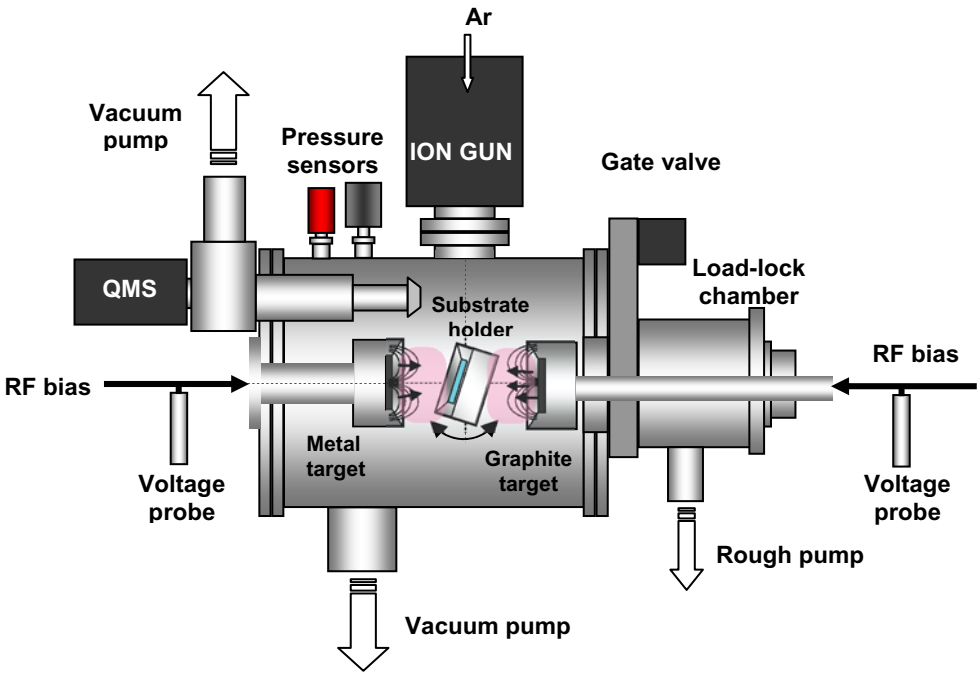


Figure 3.8: Chamber configuration with two sputtering cathodes to deposit Me/a-C multilayers by alternating magnetron sputtering of two targets.

Modulated-composition material depositions were performed by facing the holder alternatively to both targets. In order to control the deposition time of every layer, a device with a computer-controlled stepper motor was installed in the substrate holder. Figure 3.9 schematizes the configuration of the substrate holder with the stepper motor and the corresponding transmission system.

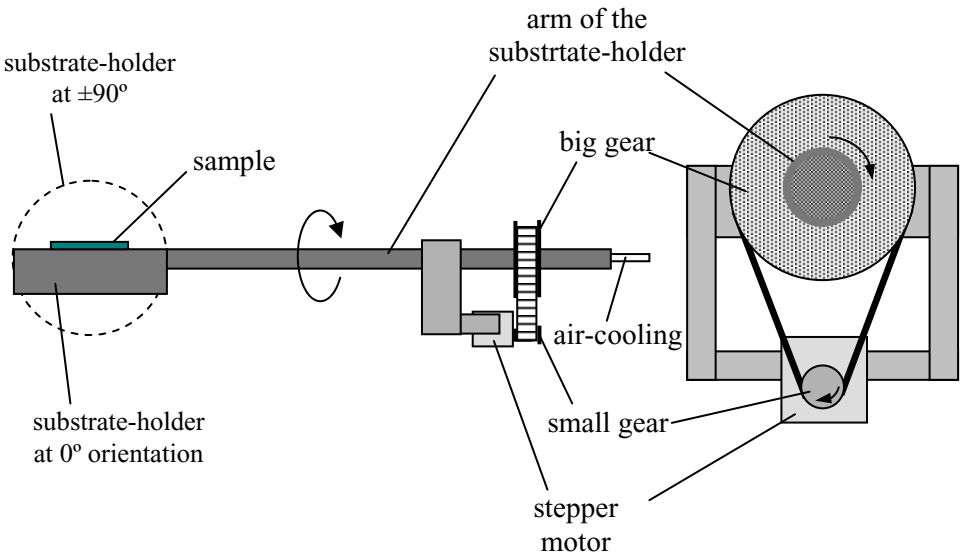


Figure 3.9: Schematic of (a) lateral and (b) frontal views of the rotatory substrate-holder equipped with a stepper motor.

Graphite was the target material used for the DLC layers deposition. On the other hand, we utilised W as metal sputtering target. As a difference with respect to the Me-DLC case, we worked in a non-reactive environment: all the depositions were run in an Ar atmosphere. The sputtering cathodes were powered through matching networks with RF generators, either in continuous wave (CW) mode or by supplying a pulsed signal consisting of square-wave modulated (SQWM) RF power.

## 3.3. Electric measurements in a glow discharge: Langmuir probe

A glow discharge or plasma can be considered in a simplified way as an ionised gas. Therefore, its characterisation is not complete if we restrict to thermodynamic variables, but it requires a richer description. Apart from gas pressure, we can define many other parameters, as for instance electron temperature and plasma potential. The determination of plasma parameters is of main importance to understand the processes involved in growth kinetics of thin films. Some works discuss the characteristics of the materials as a function of the synthesizing plasma features [Rossnagel S.M., 1987]. Furthermore, modelling of plasma fundamental processes (collisions, excitations and ionisations) is a valid tool to explain the behaviour of parameters in a concrete discharge [Alexandrov A.L., 2005].

From a glow discharge diverse information can be extracted. The measuring of ion current on a surface is carried out by a Faraday cup. Cups with special construction can provide data to calculate the energy spectrum of electrons. The light produced by desexcitations in plasma may be detected by a spectrophotometer. The distribution of emission lines in the spectrum shows a trace of elemental reactions occurred within the plasma, so the output data are discharge variables. This non-invasive technique is extensively used and is called Optical Emission Spectroscopy (OES) [Andújar J.L., 1998]. However, the most extended method for plasma diagnostics is the study of I(V) characteristics registered by an electrostatic probe, called Langmuir probe.

A Langmuir probe must be connected to a voltage supply, in order to be conveniently biased, and the current data are red by an ammeter. A typical current vs. voltage curve measured in a radiofrequency glow discharge is shown in figure 3.10. Current probe takes different values as probe voltage sweeps a determined range, thus generating a I(V) characteristic.

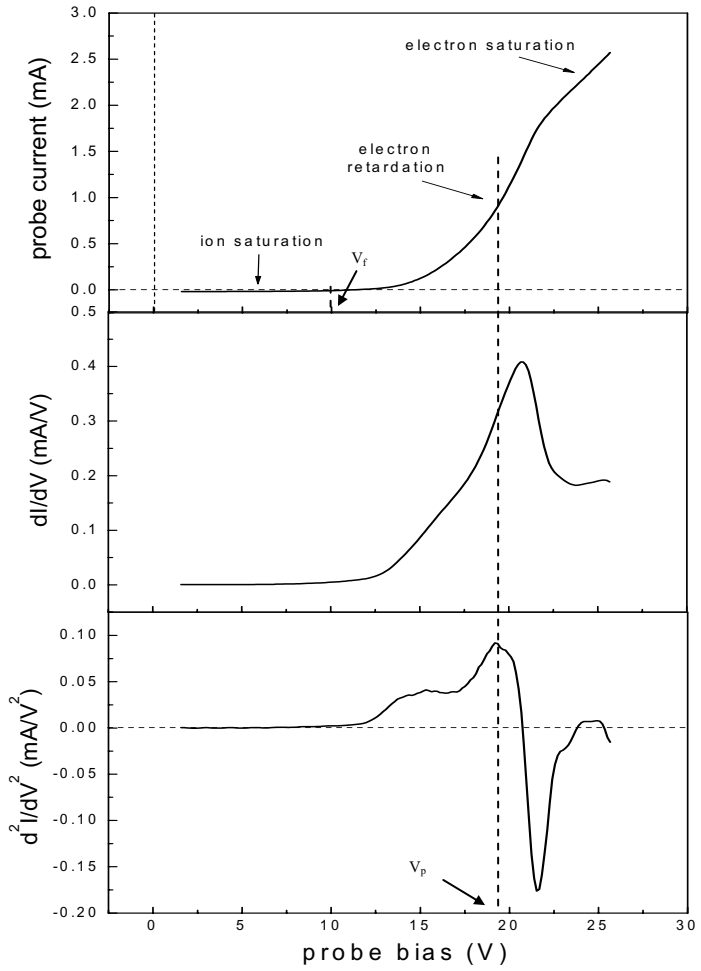


Figure 3.10: (a) typical I(V) characteristic of a glow discharge, along with its (b) first and (c) second derivatives.

Negative current values on the most left correspond to the ionic saturation current. In fact, the probe is polarised so negatively that all electron are repelled and it only detects positive ions. The current is almost constant until it goes across the X-axis. The zero current tension is called floating potential, and is interpreted as the potential where ion flux equals electron flux. Both contributions are mutually cancelled, so the probe does not measure any net current. Above floating potential there is a linear region, which is called delay zone, where electron current is the most relevant. Probe current due to electrons will be always greater than ion current, because electron mobility is very small compared with that of ions.

Plasma potential defines the inflexion point, from which the saturation of electron current takes place. This parameter can be calculated by finding the maximum of the first derivative of the I(V) or determining the zero of the second derivative.

The probe voltage, $V$, dependence on probe current, $I$, is usually modelled as follows:

$$I = I_i(V) + I_0 e^{-\frac{E}{kT_e}} \tag{3.1}$$

The first term is the ionic current, $I_i$, which turns to zero at high voltages. The second contribution is the electron current, which is constructed by the electron current at plasma potential, $I_0$; the electron energy, $E$; the Boltzmann constant, $k$, and the electron temperature, $T_e$.

The tip of a Langmuir probe is small enough to minimise intrusive effects on the discharge, i.e. the formed sheath has reduced dimensions. The geometry of the tip allows different shapes. Some of them are planar, whereas others are cylindrical [Lieberman M.A., 2005]. In this work, a tungsten cylinder of 10 mm long and 0.13 mm radius was used. The approximate insertion position is shown in figure 3.11, so the registered parameters account for plasma state in the bulk region.

The equipment of the Langmuir probe used in the laboratory (SmartProbe) consisted in a circuit box connected to the probe and to a data acquisition card. The box admitted an external trigger entrance. The card was built into a PC, and the control and reading of probe measurements were managed by the proper software. A complete I(V) *scan* was the resulting average of a determined number of I(V) measurements, which are called *sweeps*. In every sweep, it was possible to modify the number of measures per point from 1 to 1000 to perform an accurate statistics.

The lecture frequency is approximately 5 kHz, whereas the triggering signal from power supply was pulsed at 100 kHz, i.e. the pulse frequency. Moreover, the trigger from the power source is a light signal, so it must be converted to electric signal by a photodiode. The internal trigger from the probe box was not adequate to perform a synchronous data acquisition, so the additional electronic circuit shown in figure 3.11 was constructed.

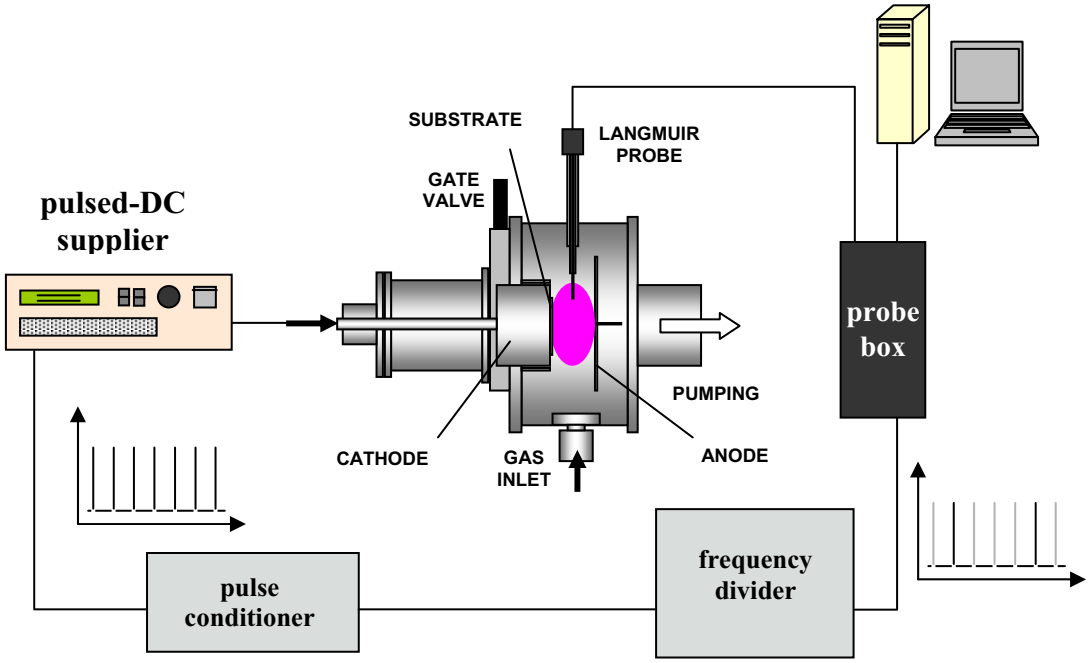


Figure 3.11: Schematic of the experimental setup for plasma data acquisition.

The light signal from the supplier was guided through an optical fibre to a photocurrent transducer, which was connected to a frequency divider. The resulting signal was amplified and led to a pulse generator with a time-delay actuator. The obtained pulses were input to the external trigger entrance of the probe box, and the I(V) scans were performed synchronous to the pulsed signal. The time evolution of the bias signal from the supply and the delayed trigger were measured by an oscilloscope. On its screen was showed the relative position of the trigger signal with respect to a pulse cycle produced by the supplier. This position was selected by acting on the time delay. The time resolution of every I(V) characteristic was 1 μs.

## 3.4. Preparation of substrates

The DLC structures were deposited onto substrates of different materials. Most of the samples consisted in films grown on (100) oriented monocrystalline silicon wafers. The thickness of the c-Si substrates was of 250, 360 or 500 μm. In general, the wafers were p-doped, but it was not relevant for the characterization (TEM, XRD, optical). However, FTIR analysis required the c-Si substrates to be impurity-free and both sides-polished.

Glass substrates consisted in microscopy holders, which were prepared by means of a cleaning protocol. They were firstly brushed with detergent. After washing them with deionised water, these holders were immersed in hot water for 4-8 hours for the softening and desorption dirty particles. Finally, the substrates were blown by compressed air and placed on the corresponding substrate holder.

Metal contacts were prepared in some samples deposited on glass, in order to study the electric behaviour by four point-probe method (see chapter 4). This was accomplished by depositing Ag electrodes with the sputtering set of figure 3.8. The used mask is shown in figure 4.8 (chapter 4). Thus, the resulting sample consisted in four rectangular contacts deposited on the DLC sample, as shows figure 3.12.

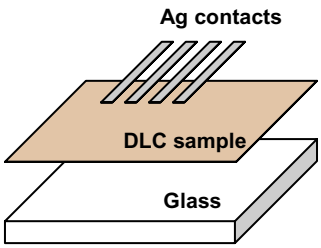


Figure 3.12: Structure of samples for electric measurements.

Gold substrates were used for ellipsometric measurements in the IR range, because the high IR reflectance of this material permits to control the transparency of the samples. The preparation of these substrates consisted in the coating of glass substrates with a gold film by means of the thermal evaporation technique. The substrates were heated to enhance sticking of Au atoms. Previously, a buffer layer of Ni-Cr was deposited at room temperature by evaporating a wire with 80% Ni and 20% Cr. The evaporation source must

be a refractory material to avoid contamination of the growing layer. We have used a tungsten crucible. Figure 3.13 shows a scheme of the evaporation equipment as well as the layering of the prepared substrates.

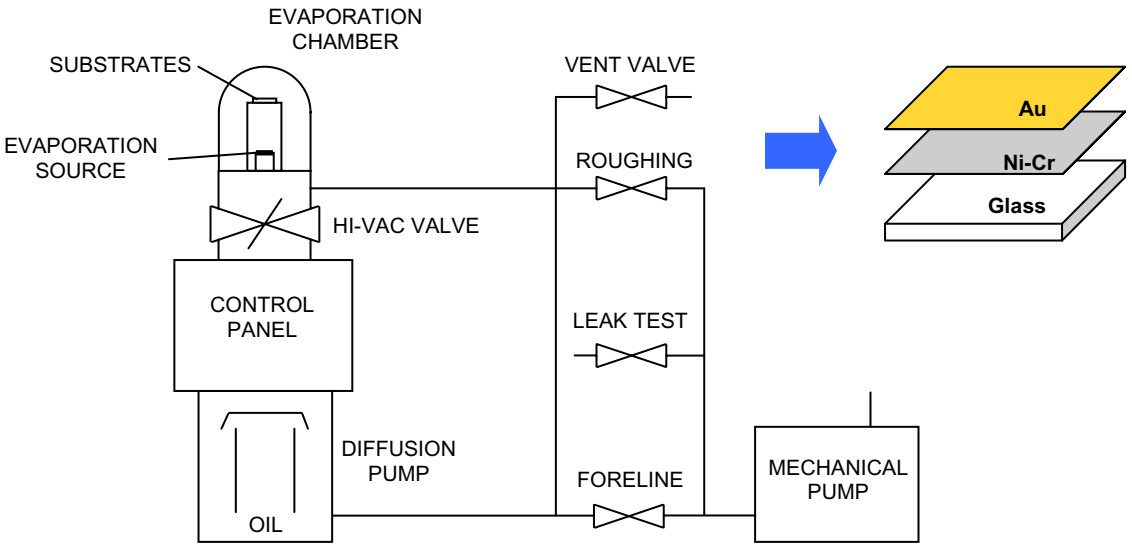


Figure 3.13: Evaporation set with its basic components and structure of substrates for ellipsometric analysis.

Evaporation is a PVD technique that requires high vacuum conditions. In order to deposit a film, the distance between the evaporation source and substrates cannot be inferior to the mean free path, $\lambda$, which is defined as the average distance crossed by the gas species between two successive collisions:

$$\lambda = \frac{kT}{\sqrt{2}\pi d^2 p} \tag{3.2}$$

where $d$ is the molecule diameter. The inverse dependence with $p$ justifies the need for an efficient evacuation. This parameter can be calculated at room temperature (25ºC) with the following expression:

$$\lambda[mm] = \frac{6.6}{p[Pa]} \tag{3.3}$$

Since substrate holder is around 30 cm over the evaporation source, pressure cannot overpass $2.2 \cdot 10^{-2}$ Pa.

# Chapter 4

# Thin film characterisation techniques

# Chapter 4 – Thin film characterisation techniques

The deposited DLC structures have been analysed by means of the characterisation techniques described below. The laboratories in which the characterisations were made are specified at the end of each section. Composition-stoichiometry and structure-morphology conform the constitutive properties, which provide fundamental information about the material. Optical response, wettability, electric, mechanical and tribological behaviours are functional properties, i.e. they suppose a control of quality for the employment of DLC in diverse applications.

## 4.1. Composition and chemical properties

### 4.1.1. X-Ray Photoelectron Spectroscopy (XPS)

In a XPS analysis, a sample is irradiated by a X-ray beam, which contains photons whose energy is $h\nu$ ($h = 6{,}63 \cdot 10^{-34}$ J·s). As a consequence, photoelectric effect is produced and, thus, the sample emits electrons with a kinetic energy:

$$E_{cin} = h\nu - E_B \qquad (4.1)$$

where $E_B$ is the energy of the electron bond, which is a characteristic of each chemical element. Free electrons pass through an electrostatic energy analyser, and a spectrum with the yield as a function of $E_{cin}$ or $E_B$ is obtained, which informs about the surface chemical composition of the sample. The incident radiation energy is higher than 1 keV, so the ionisation in the deep energy levels and the valence band is produced. Mg or Al anticathodes work as X-ray sources when they are bombarded by accelerated electrons coming from a filament. The interaction of the incident electrons with the anticathode produces a group of X-ray lines, from which only the corresponding to $K_\alpha$ is filtered for the measurements.

A XPS spectrum consists of a line distribution superposed to a background radiation. The different proportions of the areas defined by every line indicate the stoichiometry. The background increase at low kinetic energies is due to electrons with energy-loss, whereas the spectrum lines collect the electrons with full energy. Three factors contribute to line

broadening: the broadening of the radiation line, the uncertainty of the bond energy and the detection band of the instrument. The chemical shift affecting the lines is originated by the influence of the atomic environment of the probed elements. Thus, an XPS spectrum also provides information about the nature of the chemical bond. In-depth chemical profiles are measurable by varying the detection angle, and for thickness greater than nanometers, by XPS analysis combined with sputter stages with $Ar^+$.

The XPS measurements were performed in our investigations by a Perkin-Elmer PHI 5500 Multitechnique spectrometer, which was operated in the Serveis Científico-Tècnics of the Universitat de Barcelona. The X-ray sources were $K_\alpha$ lines from Al (1486.6 eV) and Mg (1253.6 eV).

### 4.1.2. Electron Probe Micro-Analysis (EPMA)

The electron microprobe is an instrument designed to determine the elemental composition of small regions of solid samples, of several cubic micrometers. The principle of operation consists on the detection of X-rays generated by bombarding the sample with a focalised beam of energetic electrons. This beam ionises the inner layers of the atoms, and consequently atomic vacancies are generated. Thus, electrons from outer layers occupy these vacancies through the emission of X-ray photons, among other phenomena, which correspond to the ionised species due to electron bombardment.

An EPMA instrument is essentially a Scanning Electron Microscope (SEM) equipped with a set of X-ray spectrometers. Figure 4.1(a) reproduces the scheme of an EPMA similar to the employed in the measurements for this thesis. It is used in the identification and quantitative analysis of a wide range of chemical elements. It can also register in digital images the different processes due to the electron interaction. As in SEM, the technique probes the sample a few microns in depth. Electrons can be absorbed, and then emit X radiation; backscattered (BSE) and directly collected by the detector; and finally, they can give rise to Auger secondary electrons, which are emitted by the sample surface as a result of electron bombardment. Figure 4.1(b) shows an example of the interaction in the volume along with some of the mentioned electron processes.

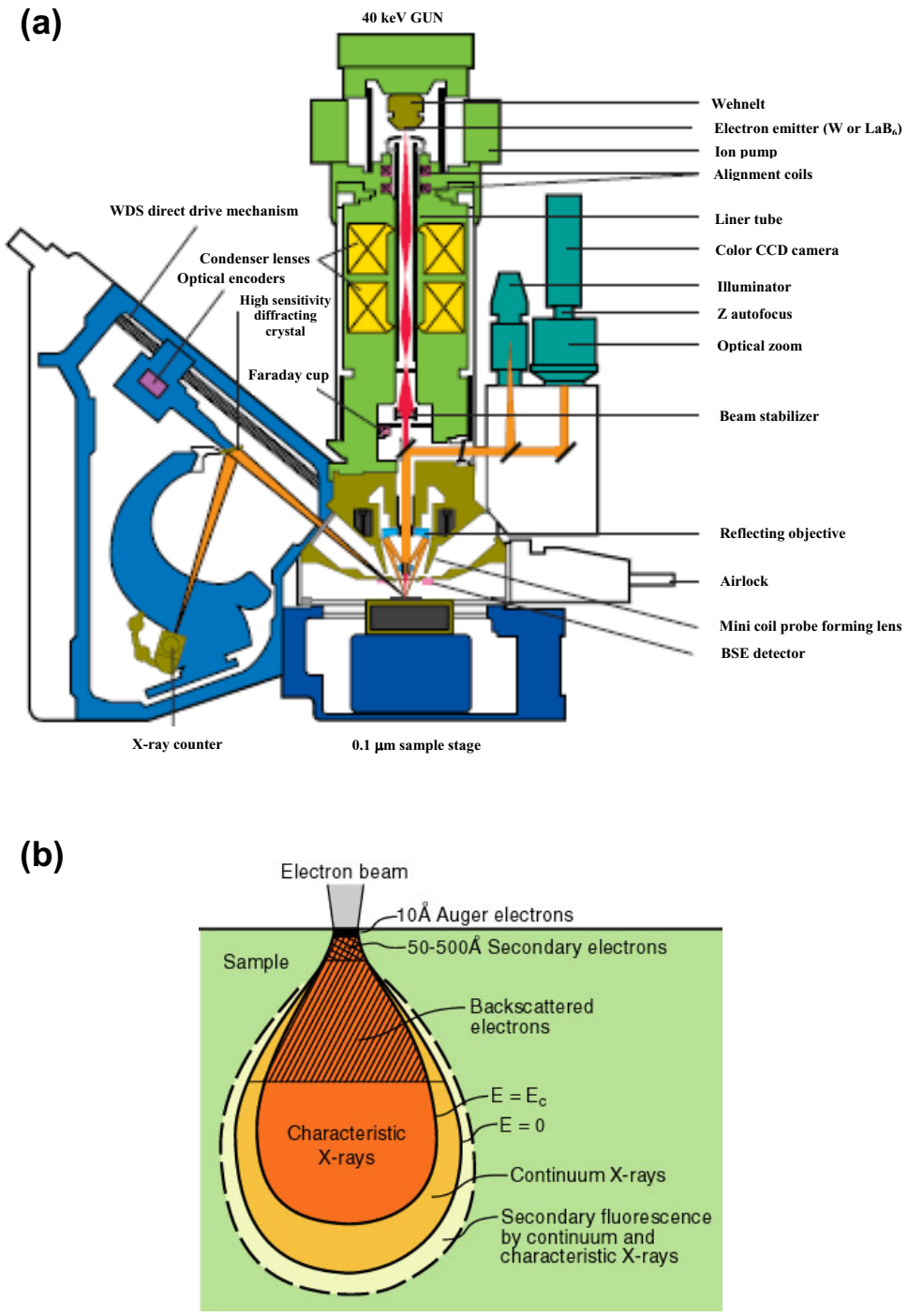


Figure 4.1: (a) Cross section view of a Cameca SX-100 EPMA, and (b) interaction volume in a sample irradiated by an electron beam.

In our case, EPMA is used for the composition analysis of thin films. X-ray spectra from the sample are obtained at different electron beam energies, which can be modified by controlling the voltage of the filament. This procedure provides the chemical composition averaged in different interaction volumes. The detected X-rays come from both the film

and the substrate. By imposing a bilayer analysing mode, the signal from the substrate can be neglected and only the film contribution is taken into account.

The EPMA measurements were performed by a Cameca SX-50 microprobe, which is equipped with four WDS (wavelength dispersion spectroscopy) and one EDS (energy dispersive spectroscopy) spectrometers. It is installed in the Serveis Científico-Tècnics of the Universitat de Barcelona.

### 4.1.3. Secondary Ion Mass Spectrometry (SIMS)

The aim of this technique is to determine the composition of a sample by analysing its emitted species due to an ion bombardment. The bombarding elements are usually oxygen or argon, whose energies range from 2 to 10 keV. As a result, surface sputtering of the sample occurs. The sputtered species are neutral, positively and negatively ionised. They can be simply or multiply ionised, and comprise atoms and polyatomic clusters. A quadrupolar mass spectrometer is employed to analyse the ejected species. It scans the charge to mass ratio abundances of the emitted ions, so the neutral species are not detected. Since the incident ions are as massive as the atoms of the sample, their interactions are very strong and a sputtering process at the surface takes place. However, the progressive removing of monolayers implies an in-depth profile of sample composition, which is an interesting aspect of SIMS for this work.

Despite the high sensitivity of SIMS to detect light elements (< 1 ppm), and its good topographical resolution, this analysis method is unable to indicate the stoichiometry of the samples. This is because we only analyse the ionised species and because, in general, the ionising probability is unknown. It depends mainly on the chemical environment or the matrix from which they are emitted [López F., 1993]. Some other disadvantages should be taken into account: mass interferences, charge-up of analysed isolator materials, and detection of adsorbed residual gases (C, H, O) on sample surface. The SIMS local analysis is performed without moving the primary ion beam, so the section size is equal to the beam one. Raster analysis mode permits to study a squared surface with areas from square microns to square milimeters.

All the SIMS analysis performed in this thesis were carried out by using an Atomika A-DIDA 3000-30, located in the Departament de Física Aplicada i Òptica of the Universitat de Barcelona.

### 4.1.4. Fourier Transform Infrared Spectroscopy (FTIR)

This spectroscopic technique for chemical analysis consists on the detection of the chemical bonds of a sample by measuring the radiation absorption bands in the near infrared (IR) range. The physical principle responsible of IR absorption is based on the exchange of dipolar momentum due to the absorption of electromagnetic radiation of a determined energy. The molecules can be studied as classic oscillators, whose basic modes are stretching and bending, when the variable is the interatomic distance or the angle subtended by the molecules, respectively. In general, the registered spectra consist on transmittance as a function of wavenumber. These measurements can be converted to absorbance and, hence, we can obtain the absorption coefficient at every wavelength. After baseline subtraction, the absorption bands are gaussian or lorentzian shaped, with their area being a measure of the absorption intensity and, therefore, of the number of bonds involved in such absorption; the line broadening informs about bond energy uncertainty, and the position is related to the kind of bond and its chemical environment. Absorption band energies of studied materials are tabulated in literature. For instance, table 5 in section 6.4 lists the IR vibrational frequencies of DLC.

The FTIR measurements were carried out by a Nicolet 5ZDX spectrometer, using a polished-on-both-sides (100) p-doped silicon substrate (50% transmittance) as a reference. This equipment is installed in the Departament de Física Aplicada i Òptica of the Universitat de Barcelona.

### 4.1.5. Raman spectroscopy

This is the most used non-destructive technique to monitor bonding in carbon materials. In this characterisation method, a monochromatic light beam is directed to the sample, and the reflected light is measured. To this end, lasers of different wavelengths may be employed. This technique is based on the physical principle of molecular vibration. Two

kinds of light scattering are possible when a photon with $hv_0$ energy collides with a molecule. Rayleigh scattering occurs when the photon frequency keeps constant after the collision. It corresponds to an elastic collision. On the other hand, Raman scattering is a process generated by inelastic collisions. The molecule is initially in the fundamental state of vibration and is then promoted to an excited state due to the accepting of the photon energy. The emitted radiation has an energy of $h(v_0 - v_v)$, which defines the radiation detected in a Raman spectrum. Unluckily, these processes are relatively not very efficient. The respective intensity ratios for Rayleigh and Raman scattering are $10^{-3}$ and $10^{-6}$. Because of this, the incident power radiation on the sample must be high enough, which can lead to its degradation due to heating. Other information extracted from Raman spectra are the mechanical stress and the graphitic character of the sample.

Macro-Raman measurements were taken in backscattering geometry with a Jobin-Yvon T64000 spectrometer using the 514.5 nm line of an Ar laser as excitation wavelength. The incident power density on the sample surface was 7 $mW/mm^2$. This instrument is located in the Serveis Científico-Tècnics of the Universitat de Barcelona.

### 4.1.6. Elemental Analysis (EA)

This is a chromatographic technique for chemical analysis. It is useful for either organic elements or amminoacids detection. The organic EA permits to identify N, C, H, S and O in materials. Such a determination is possible by means of combustion of the sample in a furnace at 1000ºC, which makes it a destructive method. The produced gases are impelled by He gas through a cavity with reactive substances, which reduce the number of gaseous species after the initial combustion. After this, the resulting gases are conducted towards a gas-chromatograph with a thermal conductivity detector, from which N, C, H and S contents in the sample are evaluated through the measurement of $N_2$, $CO_2$, $H_2O$ and $SO_2$ gases. A pirolysis of the sample employing red-hot carbon is performed in order to obtain CO and, thus, measure O concentration and complete the analysis. This method is extensively used for the study of any kind of organic compound, as well as inorganic synthesized products.

An EA 1108 CHNS-O Carlo Erba Instruments analyser was used to determine the C/H atomic ratio in a-C:H films. This equipment operates in the Serveis Científico-Tècnics of the Universitat de Barcelona.

### 4.1.7. Electron Energy Loss Spectroscopy (EELS)

This technique consists on the analysis of the energy distribution of initially monoenergetic electrons after their inelastic interaction with the atomic electrons of the sample [Rodil S.E., 2000]. EELS is usually installed in a Transmission Electron Microscope (TEM) along with a spectrometer, which consists normally on a magnetic prism that performs the filtering of electron energy. Because in TEM experiences sample thickness is thin enough to permit almost the total transmission of the electron beam, the energy loss spectrum of the electrons is intense enough to provide information about the chemical and structural properties of the specimen. Figure 4.2 shows the dispersion of electron trajectories that pass through a magnetic prism.

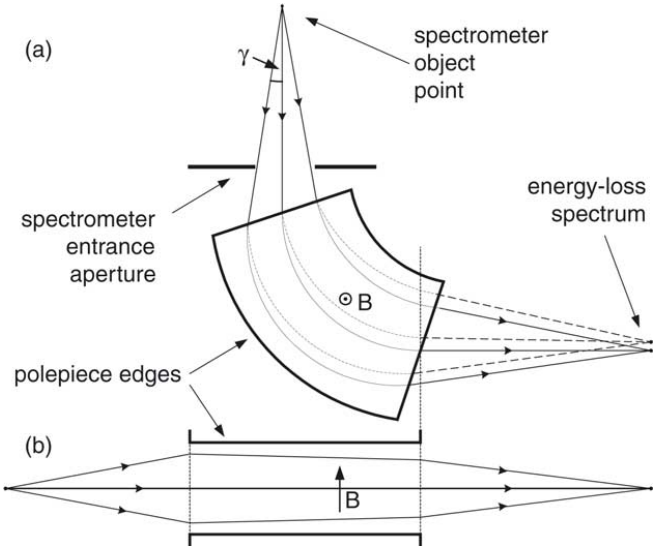


Figure 4.2: Dispersion and focusing of electron trajectories performed by a magnetic prism (a) in a plane perpendicular and (b) parallel to the magnetic field. The solid lines represent zero-loss electrons and the dashed ones represent those with lost energy.

A typical energy-loss spectrum contents two energetic intervals [Egerton R.F., 2005]. The first one involves low loss electrons, in which the zero-loss peak comprises the non-scattered or elastically scattered electrons with negligible energy loss, and plasmon peaks account for collective oscillation of the electron density within the solid. The second zone

is the core-loss region, where the intensity in the spectrum falls significantly. However, the ionization edges representing the excitation of core electrons that belong to inner atomic shells appear superimposed to this decreasing background. Since the binding energy of each shell (K, L ...) determines the edge threshold, the responsible element can be identified. Furthermore, the abundance of each element can be obtained by measuring the peak intensity of the edge.

Besides electron energy-loss spectra, electron energy-filtered TEM (EFTEM) images can be digitally recorded by means of a charged couple diode (CCD) array, which collects the photons distribution originated by a scintillator that converts the distribution of the incoming electrons. In this way, EELS results can provide both electron intensity vs. energy loss plots, and also composition mappings of the sample as obtained from the CCD camera.

EELS composition mappings were provided by a spectrometer mounted at the bottom of a Jeol 2010F TEM with field emission gun (see section 4.2), which is available at the Serveis Científico-Tècnics of the Universitat de Barcelona. Before the analysis, the samples were submitted to a plasma cleaning process carried out by a Fischione Plasma Cleaner Model 1020.

## 4.2. Structure and morphology

### 4.2.1. X-Ray Diffraction (XRD)

This is a very common technique to perform the structural characterisation of a solid material. The wavelength of the X radiation is of the order of the interatomic distances of the crystals, which act as diffraction arrays. Indeed, X-rays are diffracted in determined intensities and directions. Thus, the diffractogram of a solid is a representation of its crystalline structure. Diffraction maxima are produced when the subtended angle formed between the emergent and incident X-ray beams, $2\theta$, satisfies the Bragg's condition:

$$2d \cdot \sin\theta = m\lambda \qquad (4.2)$$

where $d$ is the distance between crystallographic planes; $m$ is a natural number, and $\lambda$ is the radiation wavelength. Peak distribution accounts for crystallographic planes parallel to the sample surface. Figure 4.3 shows the diffraction of X-rays due to the family of crystallographic planes (h k l). The incidence angle, $\alpha$, is varied by changing the sample orientation.

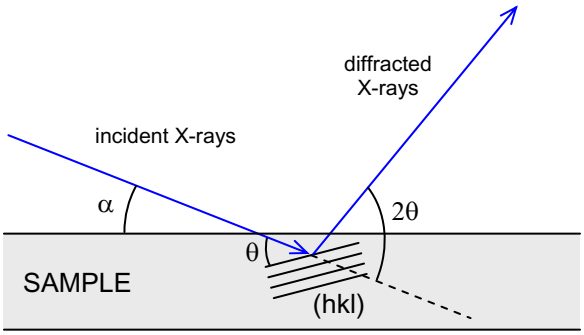


Figure 4.3: Trajectory of X-ray radiation which fits Bragg's condition with the family of planes (h k l) of a crystalline sample.

In this thesis we have focused only on $\theta/2\theta$ scans, which indicate the structure of the material when compared to the tabulated references obtained from the Joint Committee for Powder Diffraction Studies (JCPDS).

The atomic basis of a crystalline sample is responsible of the peak intensity. Indeed, the structure factor modifies the diffracted intensity. This factor is defined as follows:

$$\mathbf{S}\left(\vec{\mathbf{k}}\right)=\left|\sum_{\mathbf{n}=1}^{\mathbf{N}}\mathbf{f}_{\mathbf{n}}(\boldsymbol{\theta})\cdot\mathbf{e}^{\mathbf{i}\vec{\mathbf{k}}\cdot\vec{\mathbf{d}}_{\mathbf{n}}}\right|^{2} \tag{4.3}$$

where $k$ is the wave-vector, $d_n$ is the position of the $n$-atom within the basis, and $f_n(\theta)$ is the form factor, which informs us about the way the radiation is scattered in every direction $\theta$ by the atomic layers. The diffracted intensity, $I(k)$, is affected by $S(k)$ in the next way:

$$I(k) = S(k)Nf^{2}(k) \tag{4.4}$$

Where $N$ is the number of atoms and $f(k)$ is the atomic form for the dispersed radiation.

When the crystalline network has a high degree of symmetry, the structure factor causes systematic cancellations of diffracted intensities in some directions. Intensity and peak shape are also indicative of crystalline features. Many factors intrinsic to the measurement system (environment, instruments) modify this shape and should be subtracted to obtain only the contributions from the sample: sample absorption, its temperature, the original X-ray line shape, and the geometry of the detector.

X-Ray Reflectivity (XRR) constitutes a type of XRD analysis, where diffraction angles are taken very low. Thus, it is also called Low-Angle X-Ray Diffraction (LAXRD). Reflectometry is effective for the study of films with poor crystallinity, as for instance, amorphous materials with embedded nano-crystals. In this way, low angle incidence provides more fraction of the X-ray beam to be diffracted, which increases the signal to noise ratio. Many film characteristics may be achieved by a simulation process of XRR diffractograms. Morphologically, we can calculate film thickness and surface roughness. Film density and compositional data are other output parameters. A more detailed description of this method can be found in chapter 6.

XRD and XRR scans were obtained with a SIEMENS D-500 diffractometer with a θ/2θ Bragg-Brentano geometry, operating at a wavelength of 0.15406 nm. Furthermore, XRR diffractograms were performed in high-resolution operating mode. All the diffractometers are located in the Serveis Científico-Tècnics of the Universitat de Barcelona.

### 4.2.2. Transmission Electron Microscopy (TEM)

Electron microscopy is a widely used technique to inspect the morphology of a sample with high resolution. Optical microscopes are not able to resolve features smaller than the shortest wavelength of visible light, which is around 400 nm. Thus, imaging at very small scales is to be performed by means of the radiation of an electron beam, whose associated wavelength, $\lambda$, can be reduced by four orders of magnitude with respect to the optical wavelength. In fact, such associated wavelength is determined by the kinetic energy of the electron, $K$, which follows de Broglie's expression:

$$\lambda = \frac{h}{p} = \frac{h}{\sqrt{2mK}} \tag{4.5}$$

where $h$ is the Planck's constant, $p$ is the momentum of the electron, and $m$ is the electron mass. The electron microscopes that image the sample in transmission mode are called TEM, and they require sample thickness in the 100-200 nm range or thinner. On the other hand, Scanning Electron Microscopes (SEM) operate by detecting mainly the electron scattered on the sample surface, which puts no thickness limitations.

In this thesis we have studied the morphology and the structure of the films by cross-section TEM observations. The following section describes how the samples were prepared.

**· Sample preparation for cross-section TEM analysis**

(i) Sample cutting:
TEM observations have been made on films deposited onto c-Si. A sample for TEM must be cut with a Cu rotating saw coated with diamond micrograin, in order to obtain two rectangles of approximately 2.5 mm x 1 mm. Samples like ours can then be cleaned with acetone.

(ii) Glued pairs (figure 4.4):
These two pieces are glued with polymeric glue (M-bond) by facing the coated surfaces, and must remain on a hot surface (100ºC) and pressed by means of inverted tweezers

typically for 4 hours. Eventually, a specimen may easily break during sample preparation, and to that extent several of these sandwiched specimens are processed in each preparation.

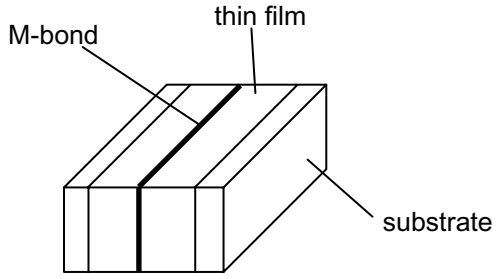


Figure 4.4: Schematic of a glued pair for TEM observation.

(iii) Plano-parallel grinding:

The specimen is then stuck on a disc grinder, and is ground with a SiC paper of 30 μm grain size until sample is around 0.5 mm thick. After that, it must be polished using papers with finer grain (15, 3, 1 and 0.3 μm) until it presents a mirror-like appearance. In this part, an optical microscope reveals very helpful.

(iv) When the sample is polished enough, it must be detached (with acetone) and then reversed and stuck again on the center of the grinder. Next, step (iii) must be repeated until the sample is around 50 μm thick wafer.

(v) Concave grinding:

An ultra-thin area is produced by performing a dimple grinding. As a result, a crater appears in the middle of the sample whose center should be 30 μm thick at the end of this step.

(vi) Ring mounting:

TEM sample holder consists of a copper disc with a centred and narrow overture. The dimple-ground specimen must be carefully glued on this holder by means of the polymeric glue. After several minutes heating, the sample is ready for the next step.

(vii) Ion milling:

The specimen should be placed on a special holder and ion milled in an ion milling system (Precission Ion Polishing System - PIPS), until a centred hole is produced. The electron-

transparent zones, thinner than 100 nm, are adjacent to this hole. This last step is critical and should be carefully controlled.

Figure 4.5 shows an overview of the preparation process of a TEM sample after the "sandwich" is done.

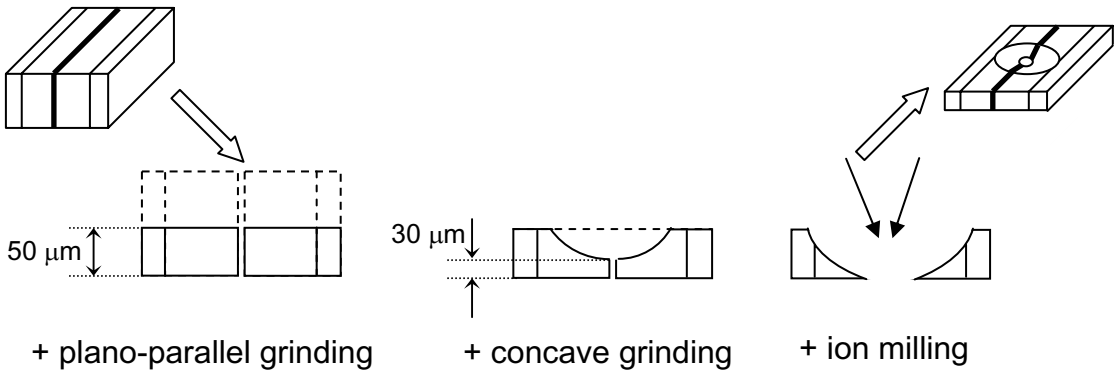


Figure 4.5: Different stages of the preparation process of a TEM sample.

TEM is the only technique able to characterise the microstructure of materials and at the same time it provides crystallographic information from selected regions of the sample. Sample images come from the collection of electrons scattered in the material. Such images are normally constructed with the beam of transmitted electrons, and are called *bright field* images. On the other hand, *dark field* images are generated only from diffracted beams in specific angles. In this case, the transmitted beam is intercepted and we can only observe diffraction contributions all over the sample. Figure 4.6 shows a schematic picture of a TEM column.

Conventionally, such system is composed of an electron gun, several electromagnetic lenses to focalise, deflect or magnify the electron beam, and an adjustable substrate holder. The electron source consists normally of a W or $LaB_6$ filament, or eventually a field emission gun. Selected Area Electron Diffraction (SAED) patterns are obtained by using the diffraction lens and acting on the selected area aperture. Such diffractograms fulfil the Bragg's law, as in the XRD case (see equation 4.2). The only difference is the radiation wavelength: X-rays have a wavelength in the order of 0.1 nm, while the wavelength of 200 keV electrons is about $10^{-3}$ nm. By following Bragg's law, we infer that X radiation

diffracts with an angle of some tens of degree in front of a plane spacing of 1 nm, whereas diffraction angles of electrons are a hundred times smaller.

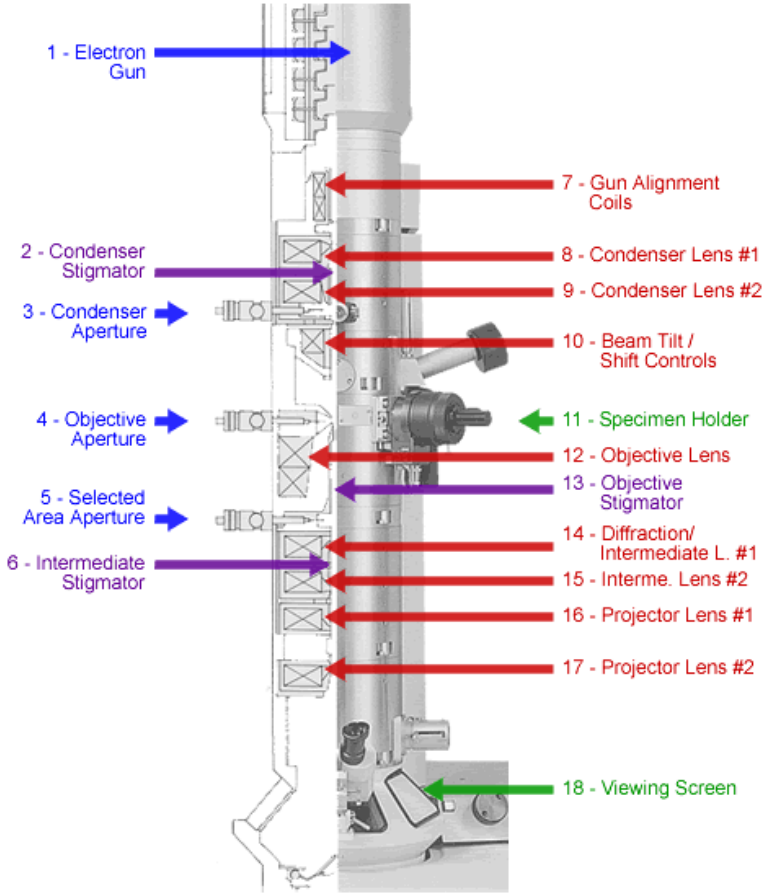


Figure 4.6: Schematic view of a TEM column.

For small angles, $sin\ \theta$ can be approached to $\theta$. Thus, for Bragg reflections of first order, the equation 4.2 is as follows:

$$2d \cdot \theta = \lambda \tag{4.6}$$

If we define $R$ as the distance between the transmitted and the diffracted beam on the photographic plate, whose distance to the sample is $L$, equation 4.6 changes to:

$$Rd = \lambda L \tag{4.7}$$

where $\lambda L$ is the camera constant of the microscope. Hence, the knowledge of this constant and the measurement of $R$ permit us to calculate the spacing of planes, $d$.

The main application of TEM is addressed to the study of materials and the imaging of their morphology. High resolution TEM (HRTEM) images can show the atomic

distribution in a crystalline material. In this case, an accurate beam alignment and a minimisation of aberrations are mandatory. Through SAED diffractograms one can determine the material structure (amorphous or crystalline), the identity and orientation of a monocrystal, and the relative orientation between two phases.

Cross-section TEM micrographs and SAED patterns were obtained by a Philips CM30 electron microscope operated at an accelerating voltage of 300 kV. HRTEM images and EELS composition mappings were provided by a Jeol 2010F field emission TEM equipped with an energy filtering device.

## 4.3. Electric properties

### 4.3.1. Four point probe method

The electric conductivity of a thin film, deposited onto an insulating substrate, can be measured by an ohmmeter operating in the two point probe mode. In this case, the measurement is partially masked as it comprises the contact-resistance between sample and electrode. Four point probe measurements are preferred as they have no parasitic contribution. In this case, two outer probes inject current and the other two read the electric tension. They are normally configured in line, as schematized in figure 4.7.

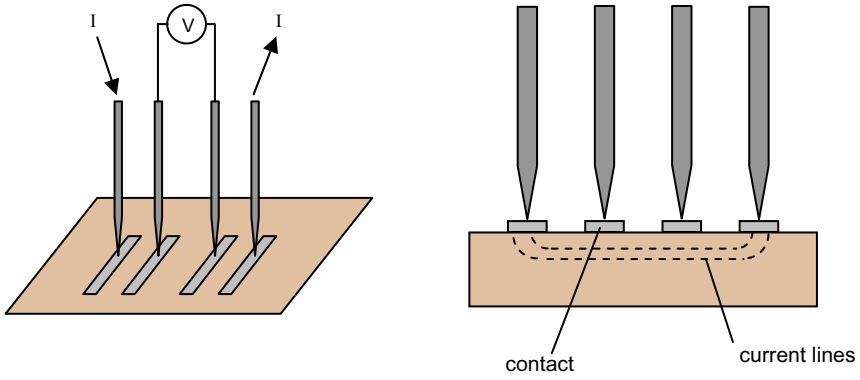


Figure 4.7: Four-point configuration for the measurement of electric conductivity.

The sheet resistance, $R_{\square}$, is a widely used parameter to characterize the electric properties of thin films. If we define a square section of a thin film with thickness $d$, the electric resistance measured orthogonally to the substrate does not depend on the square size, but only on the film resistivity, $\rho$:

$$R_{\square} = \rho / d \tag{4.8}$$

In our measurements, the electric contacts consisted on aluminium rectangles deposited by magnetron sputtering of an Al target. Their dimensions and spacing are shown in figure 4.8. Since the contacts are spaced 1 mm and the film thickness is smaller than 1 μm, it is a good approximation to suppose that the current lines are not distorted near the contacts and that the current propagation across the film is homogeneous.

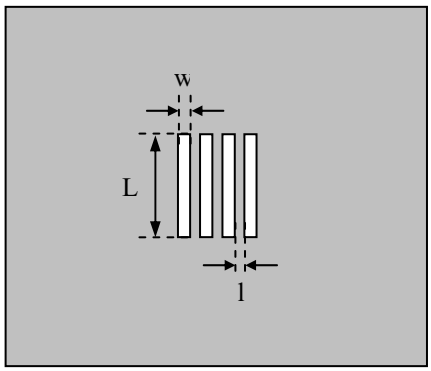


Figure 4.8: Mask designed for the deposition of electric contacts onto surfaces.

These electric measurements were carried out employing a current injector, a voltmeter, and a sample holder connected to a heater. This system is available in the Thin Films Laboratory of the Departament de Física Aplicada i Òptica of the Universitat de Barcelona.

### 4.3.2. Scanning Electrochemical Potential Microscopy (SECPM)

SECPM consists of a special case of Scanning Potential Microscopy (SPM). It offers an in-situ potential mapping of a surface acting as an electrode in the X,Y plane, with a nanometer-scale lateral resolution. The instrument is composed of a potentiostat that controls the difference of electric potential of a conductive sample with respect to a Pt/Ir potentiometric probe immersed both in an electrolyte solution. The electric field propagates inside the liquid medium and it can be sensed by the probe through the electric potential distribution. The probe can operate in three modes: constant potential mode, where topographic scans are captured; constant height mode, to map the electrochemical potential distribution across the sample surface; and the spectroscopic mode, where the X,Y raster is substituted by the Z scanning and we obtain the electric potential vs. the travelled distance. In this work, the constant height mode with a high lateral resolution was employed to map the metallicity throughout the film surface with a high lateral resolution.

SECPM measurements were performed by a series of SPM from Digital Instruments, available in the Serveis Científico-Tècnics of the Universitat de Barcelona.

## 4.4. Optical properties

### 4.4.1. UV-visible transmittance

The spectral study of the light transmitted by a film/substrate system gives us information about the optical parameters of the film. The visible light consists on electromagnetic radiation with wavelengths, $\lambda$, comprised between 400 (violet) and 750 nm (red). The light intensity is proportional to the square power of the amplitude of such electromagnetic waves. The optical transmittance spectrum, $T(\lambda)$, is defined as the ratio between transmitted, $I$, and incident light intensities, $I_0$, at each point $\lambda$ of the optical spectrum. In the case of a low-absorbent thin film deposited onto a non-absorbent substrate with refractive index $n_s$, as for instance glass, the fitting of $T(\lambda)$ curve in air ($n_0$=1) by a certain model provides refractive index, $n$, absorption coefficient, $\alpha$, and film thickness, $d$, according to the following expression [Swanepoel, 1983].

$$T(\lambda) = \frac{16n^2 \cdot n_s \cdot n_0 \exp(-\alpha \cdot d)}{(n+n_0)^3(n+n_s^2) - 2(n^2-n_0^2)(n^2-n_s^2)\cos(\frac{4\pi \cdot n \cdot d}{\lambda})\exp(-\alpha \cdot d) + (n-n_0)^3(n-n_s^2)\exp(-2\alpha \cdot d)} \quad (4.9)$$

If the film presents stronger absorption, the Lambert-Beer expression may be an acceptable approximation for the $T(\lambda)$ behaviour:

$$I(\lambda) = I_0 \cdot e^{-\alpha(\lambda) \cdot d} \quad (4.10)$$

In our measurements of $T(\lambda)$, the analysed light is emitted by a halogen lamp and is directed through an optical fibre to the sample holder. The transmitted light is then guided to a spectrograph followed by a 1024 diode array detector (Oriel Instaspec III), which detects the light intensity in the range between 300 and 800 nm.

The optical characterisation set is mounted in the Departament de Física Aplicada i Òptica of the Universitat de Barcelona.

### 4.4.2. UV-vis-IR spectroscopic ellipsometry

Ellipsometry determines the optical properties of thin films and materials with high precision. It measures the variation of the polarisation state of a light beam, as a

consequence of its reflection on the sample surface. The ellipsometric angles are $\Psi$ and $\Delta$, which are defined as follows:

$$\frac{R_P}{R_S} = \tan(\Psi)e^{i\Delta} \tag{4.11}$$

where $R_P$ and $R_S$ are the reflectances in the parallel and transversal directions to the incidence plane, respectively. The complex dielectric function of the film can be obtained through a model considering a semi-infinite medium with a previous layer, which contains information about the surface roughness.

The UV-visible ellipsometric characterization, in the range from 1.5 to 4.1 eV, was carried out using a multichannel Rotating Analyser Ellipsometer (RAE) at an angle of incidence of 70º. Figure 4.9 presents a scheme of this ellipsometer. The light source is a Xe lamp (75 W) and the polarizer is set to an azimuth of 45º of the plane of incidence. The light reflected by the sample passes through the analyser and an optical fibre guides it to the spectrophotometer. The ORIEL Instaspec III spectrophotometer can detect a full spectrum in 20 ms at 16 fixed positions of the analyser. Fourier analysis of the light intensity at each wavelength, after subtraction of the background signal, provides us with the spectroscopic ellipsometric angles, Ψ and Δ. This system allows measurements of low level signal. In this case, the diode array detector is cooled in order to increase the signal to noise ratio, and is purged with dry nitrogen to remove water vapour from the array and the quartz window of the light source.

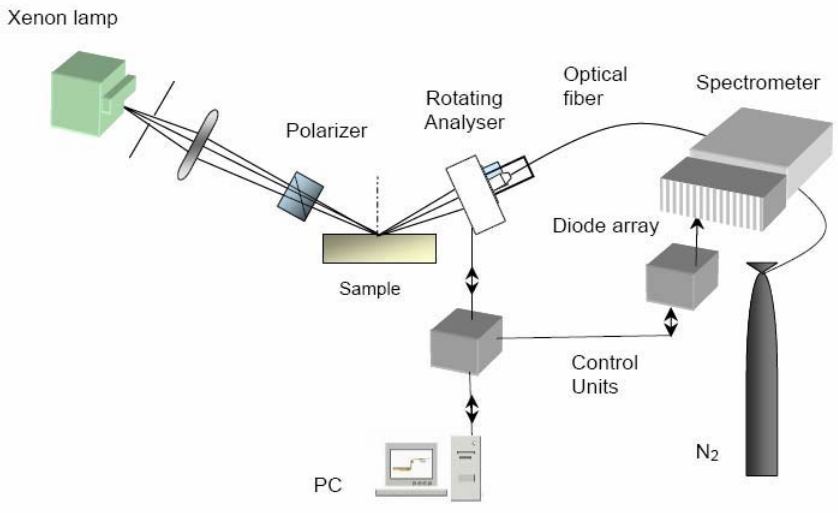


Figure 4.9: Schematic of the multichannel rotating-analyser ellipsometer.

Our IR ellipsometric spectra were obtained in the range from 900 to 3500 $cm^{-1}$, with 8 $cm^{-1}$ of resolution, at an angle of incidence of 72.5º, with an integration of 400 interferograms. The measurements were performed by a Fourier Transform Phase-Modulated (FTPME) Jobin Yvon ellipsometer that takes advantage of an optimized calibration method [Canillas A., 1993] [García-Caurel E., 1999]. $\Psi$ and $\Delta$ were measured with high accuracy by registering the spectra corresponding to three different configurations of the modulator (M) and analyser (A) optical elements: C1 (M=-45º, A=+45º), C2 (M=-45º, A=-45º) and C3 (M=0º, A=+45º).

Both ellipsometers are available in the Departament de Física Aplicada i Òptica of the Universitat de Barcelona.

## 4.5. Mechanical, tribological and topographical properties

### 4.5.1. Profilometry (thickness and intrinsic mechanical stress)

The 1-D surface topography of a sample can be measured with a profilometer. This instrument is basically used to study the surface roughness due to its high vertical resolution, in the order of 0.1 nm. In contrast, the horizontal resolution is poor, as the normal profile scans require some millimeters to be taken. A diamond tip joined to a lever transmits the topographic features to a capacitance, which acts as an electric transducer.

Profilometry can be applied in many ways. The film thickness can be estimated by measuring the height of a step formed on the surface. To produce the height-steps, in our case, a marker was used to produce a few ink dashes on the substrate surface. After the growing process, both the material deposited on the marks and ink were lifted-off by ethanol, and then an array was produced and allowed to obtain a good estimate of the local film thickness.

Furthermore, profilometry is adequate to measure the substrate bending due to mechanical stress of the film. This parameter is calculated from Stoney's equation [Stoney G.G., 1909]:

$$\sigma = \frac{Y_S \cdot t_S^{\,2}}{6 \cdot (1 - \upsilon_S) \cdot t_C} \left( \frac{1}{R} - \frac{1}{R_0} \right) \tag{4.12}$$

where $\sigma$ is the intrinsic mechanical stress; $Y_S$ is the Young's modulus of the substrate; $t_s$ is the substrate thickness; $\upsilon_s$ is the Poisson's coefficient of the substrate; $t_c$ is the film thickness (step height); $R$ is the curvature radius of the film/substrate system, and $R_0$ is the curvature radius of the substrate without film. From this, we can infer that tensile stress (concave) is positive, and that compressive stress (convex) is negative. Figure 4.10 shows a scheme of a compressively-stressed substrate.

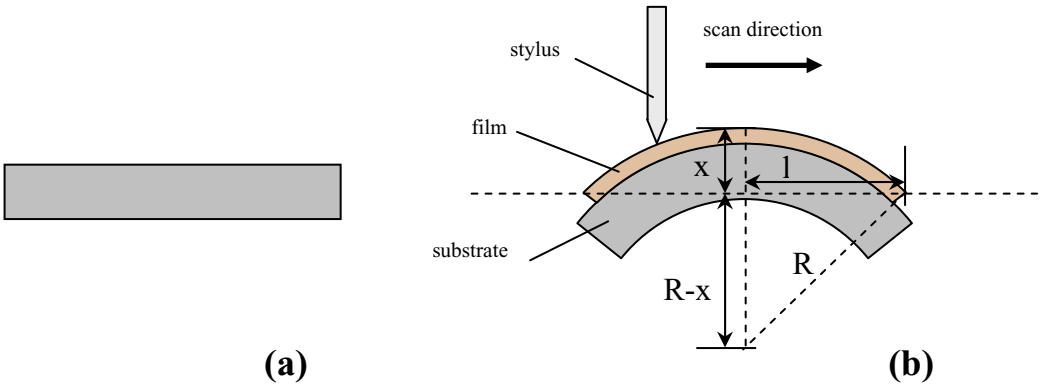


Figure 4.10: Lateral view of (a) a bare substrate and (b) a compressively stressed one due to the deposited film.

Poisson's coefficient is approximately 0.33 for all solid materials, and indicates the broadening of a pressed solid material in the orthogonal plane of pressure direction. Young's modulus of Si is 47 GPa. If we assume that the substrate height over a horizontal plane, $x$, is negligible if compared to the scan distance, $2l$, we find that curvature radius is inversely proportional to this height:

$$R = \frac{l^2}{2x} \tag{4.13}$$

For our measurements we usually took $2 \cdot l = 10$ mm.

The Dektak 3030 profilometer used for this measurements is available in the Departament de Física Aplicada i Òptica of the Universitat de Barcelona.

### 4.5.2. Atomic Force Microscopy (AFM)

This technique permits to study the surface topography of a sample with atomic vertical resolution. It is based on the repulsive and attractive atomic forces experienced by a cantilever, when its sharpened tip is brought within atomic distances above the sample surface by moving either the sample with piezoelectric transducers or the scanning head of the AFM. These forces are of the order of $10^{-8}$-$10^{-6}$ N. The forces in which AFM is based are universal. For example, the analysis of insulating samples is here possible, as compared to the case of Scanning Tunnelling Microscopy (STM).

The atomic forces can be of short and long range. Short range interactions are repulsive and manifested at a distance of about 0.1 nm, due to the proximity of the electron orbitals in the sample with those at the cantilever surface. Long range interactions dominate when the AFM tip and the sample surface are separated around 1 nm, and can be attractive and repulsive (electric, magnetic), or just attractive (Van der Waals).

There are three main operation modes for an AFM: contact, non-contact and tapping. Contact mode is normally destructive because it implies the scratch of the tip against the sample surface. Here, the bending of the cantilever transmitted by the surface features deflects a laser beam, whose spot points to a screen that registers the signal evolution. Figure 4.11 illustrates such measurement process with an AFM. In non-contact mode, the tip scans the surface between 1 and 2 nm away from it. The main interactions are attractive, so the measurements should be made very carefully in order to avoid the crush of the tip towards the surface. The most used mode is tapping. In this case, the cantilever oscillates at a characteristic resonant frequency, with amplitude of hundreds of nanometers. Thus, tapping mode gives information about topography and eliminates the surface wear due to damage to the cantilever tip, because now the contact is not constant, but intermittent.

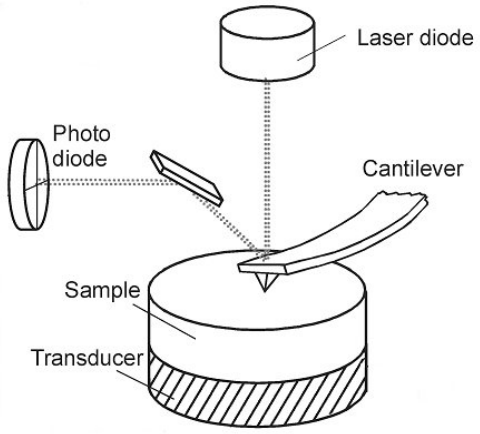


Figure 4.11: Schematic of the operation principle of an AFM. Laser deflection owes to the deformation of the cantilever, which transmits surface features.

A conventional parameter found out by AFM technique is surface roughness, which is a measure of the heights distribution in the Z direction, orthogonal to the surface plane. However, a common definition of surface roughness is the root mean square from the average height within a scanned surface, $R_{RMS}$:

$$R_{RMS} = \sqrt{\frac{\sum_{i=1}^{N}(Z_i - Z_{ave})^2}{N}} \tag{4.14}$$

where $N$ is the number of points measured on the surface, $Z_i$ is the height of the i-point, and $Z_{ave}$ is the average height of the plane.

The AFM measurements were performed with a Nanoscope IV from Digital Instruments operated in tapping mode, available at the Serveis Científico-Tècnics of the Universitat de Barcelona.

### 4.5.3. Contact angle

Wettability is a surface characteristic that should be minimized in materials for fluid-contacting applications. The physical parameter that describes it is the surface energy, and is estimated by contact angle measurements. The following expression is considered when a sessile drop is deposited onto sample surface:

$$\gamma_{sg} = \gamma_{sl} + \gamma_{lg}\cos\theta \tag{4.15}$$

where the surface energies correspond to the solid-gas interface, $\gamma_{sg}$, to the liquid-gas interface, $\gamma_{lg}$, and to the solid-liquid interface, $\gamma_{sl}$. The contact angle, $\theta$, is defined as shown in the figure 4.12, and gives a measurement of the material hydrophobicity. A material is hydrophobic ($\theta > 70^{o}$) or hydrophilic ($\theta < 70^{o}$) when it presents low or high wettability, respectively.

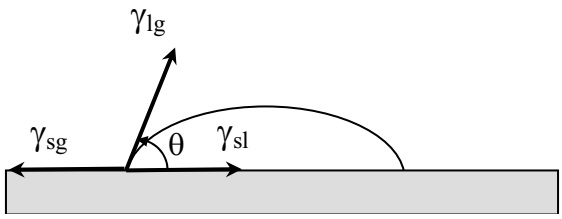


Figure 4.12: Definition of the contact angle of a sessile drop deposited onto a sample. The force vectors due to the surface energies $\gamma_{sg}$, $\gamma_{lg}$ and $\gamma_{sl}$ are also represented.

The contact angle can be measured with different techniques. In this work, the sessile drop and Wilhelmy plate methods were used. The former consists of analysing the lateral image of the sessile drop deposited onto a surface. The Wilhelmy plate method is the most used

to obtain the equilibrium surface tension of liquid samples. In our case, a solid sample that is hung on a dynamometer is slowly dipped in a liquid, whose surface tension is known. Figure 4.13 shows a sketch of the measuring procedure. The measuring cycle is completed when the sample is retracted from the liquid to the initial position. Then, the contact angle is found out by measuring, at different immersed areas, the wetting force exerted by the liquid to the sample. For these measurements, the sample must be previously cut and glued in a "sandwich" configuration with the deposited areas facing outwards. The resulting sample configuration consists of a structure of film/substrate/glue/substrate/film, as shown in figure 4.13. The procedure to determine the contact angle is described in chapter 6.

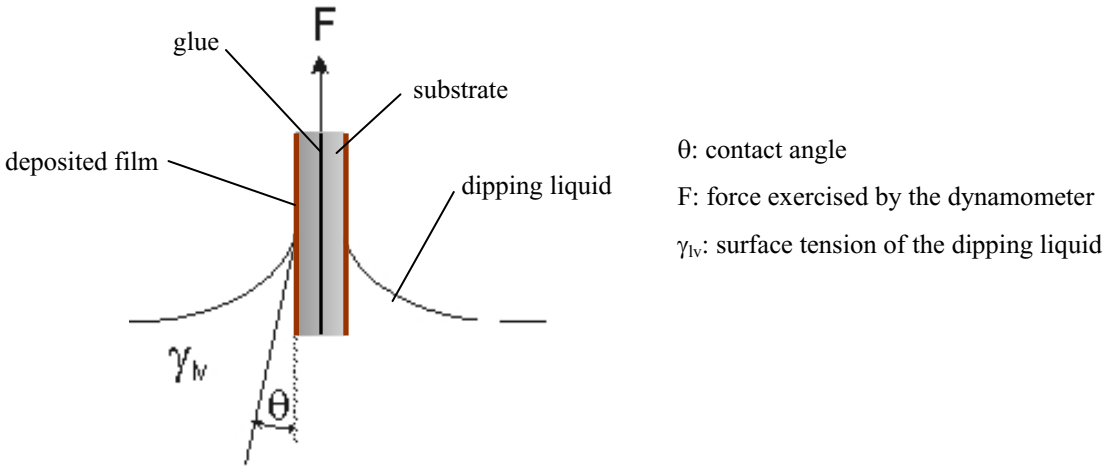


Figure 4.13: Definition of the contact angle measured with the Wilhelmy plate method.

Contact angle of the sessile drop was measured with an Optical Contact Angle Meter CAM200 from KSV, which is installed in the Departament de Física Aplicada i Òptica of the Universitat de Barcelona. The equipment used for contact angle measurements with the Wilhelmy plate method was a Sigma 20 tensiometer, employing $H_2O_{mq}$ as the dipping liquid. This instrument is located in the Departament de Tecnologia de Tensioactius of the IIQAB-CSIC.

### 4.5.4. Nanoindentation

This is a commonly accepted method used to determine the hardness of a thin film avoiding its delamination and without considering substrate effects. In order to minimize the influence of the substrate, the indentation depth cannot be greater than 25% of film

thickness. Actually, a statistical method has been applied in order to discard any possible influence of the substrate during the load cycles. The area of the indentator trace is deduced from the measured load-depth curves and is correlated with the film hardness.

Figure 4.14 shows a scheme of the measuring system (NanoTest 550). It consists of a pendulum, which is subjected at medium height by a pivot. The sample is subjected on a motor-equipped vertical holder. The positioning and motion of the sample is driven by three motors with XYZ configuration. The inclination of the pendulum is set through the force exerted by the coil at the top by varying the circulating current in the electromagnet. The limit stop defines the maximal elongation of the pendulum towards the sample. Indentation depth is then measured through the plate separation of the capacitance transducer placed in front of the indenter.

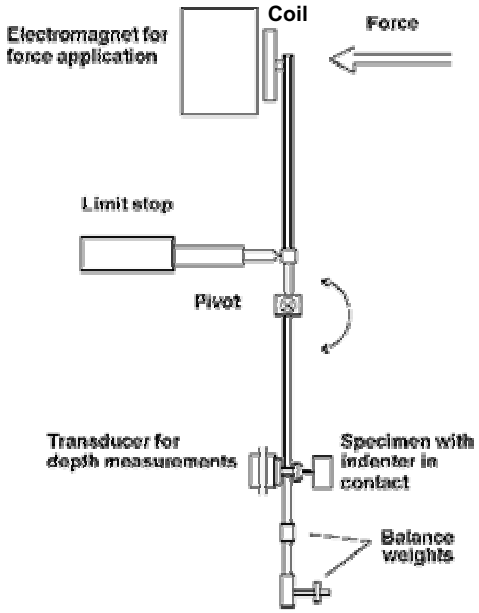


Figure 4.14: Schematic of the nanoindenter NanoTest 550.

The micro-hardness of the DLC structures was studied through the nanoindentation method using a NanoTest 550 (MicroMaterials) characterisation system, which is installed in the Departament de Física Aplicada i Òptica of the Universitat de Barcelona. It was fitted with a sharp Berkovich diamond indenter with a tip radius of 200 nm. Indentation curves were obtained with loading and unloading rates of 0.056-0.56 mN/s. The hardness of the coatings was calculated from load-penetration curves using the analysis method of Oliver and Pharr [Oliver W.C., 1992]. The applied load was varied from 1.5 to 12 mN.

### 4.5.5. Friction coefficient and micro-scratch

The scratch test is the most used technique to evaluate the adhesion of a thin film deposited onto a substrate. It consists on sliding a diamond tip on the film surface. The tip is normally a sphere of about 0.2 mm radius. A force normal to the substrate plane, or load, is applied and gradually increased until the layer is not adhered any longer and, then, is drawn from the substrate. At this point, the *critical load* is achieved. It constitutes a figure of merit that indicates how hard and well-adhered a film is. However, these results depend on a series of variables, classified into intrinsic and extrinsic parameters. Intrinsic parameters concern instrumental set-up (tip radius, scan velocity), whereas extrinsic ones are related to the analysed system (surface roughness and thickness). Substrate deformation in scratch test generates many tensions within the system film/substrate. One of the induced forces is tangentially applied to the interface of this system. When the critical load is reached, this tangential force equals the tangential mechanical resistance of the interface and induces the film failure. The type of failure and the critical load depend on the parameters mentioned above.

Complementary measurements of the friction force between the sliding tip and the film surface can be performed in scratch tests. A resistors bridge installed on the tip cantilever detects its deformation, which is proportional to the tangential force exerted by the film surface. We obtain the friction coefficient by determining the ratio between friction force and load (normal force).

The critical load is determined not only by observing with optical microscopy the track marked by the ball. To this end, the scans of friction coefficient vs. applied load are also useful. Before film cracking, friction coefficient is almost constant and can be measured. A discontinuity in this value establishes the critical load. In order to get more accurate values of the critical load and classify the type of material failure, SEM observations are needed. They are also of valuable interest to study the failure zone in more detail.

Scratch tests were carried out by the scratch header of the NanoTest 550 system, constructed by Micro Materials Ltd. It can apply loads up to 20 N and measure depths of

the order of microns. This instrument also measures hardness by nano-indentation and is installed in the Departament de Física Aplicada i Òptica of the Universitat de Barcelona.

### 4.5.6. Lateral Force Microscopy (LFM)

The AFM configuration can be modified to perform nano-tribology measurements. This technique, which was firstly developed by Mate et al. (1987) at IBM Almaden Research center, provides local data about tribology and is very useful for wear and scratch tests in ultra-thin coatings [Bhushan B., 1999b]. The instrument is set to scan the sample surface in contact mode and the load force applied to the cantilever is controlled. Thus, added to the topographical data we obtain the friction force exercised by the surface to the cantilever tip due to their interaction.

The laser beam deflection indicates both surface profile and cantilever torsion. Indeed, the horizontal and vertical forces are determined by multiplying the cantilever deflection by the spring stiffness of the cantilever in each direction. In order to reduce hysteresis on the piezoelectric actuators, scanning transversal to the long axis of the cantilever is preferred [Ruan J.-A., 1994]. In our measurements, average values of friction coefficient were inferred from lateral to load force ratios obtained at different loads. Friction force mappings of the sample surface could also be registered to get a qualitative distribution of friction domains.

LFM scans were performed by a Nanoscope IV AFM from Digital Instruments, equipped with a $Si_3N_4$ cantilever containing a 100 nm radius tip that scanned, in contact mode, 200 nm long tracks at a frequency of 1 Hz. The AFM was installed in a controlled-atmosphere chamber, since these measurements are very sensitive to temperature and relative moisture of the environment.

### 4.5.7. Calo-wear test

This is an appropriated technique to find out the thickness and the wear rate of thin films. As shows figure 4.15(a), a hardened steel ball is leaned against the sample surface, which is fixed on a holder. A suspension of $Al_2O_3$ powder (1 μm) in glycerine is used

(glycerine-$Al_2O_3$ ratio of 0.33). A droplet of suspension is added on the surface of the ball, which is placed onto a rotating stage that will turn until the film is worn enough. Then, if the ball has not reached the substrate and the sample has not been delaminated, the volume of the generated crater is directly related to the wear rate of the film. Figure 4.15(b) shows a cross-section scheme of this crater. When making the crater in the sample, some parameters must be set to given values. The following formula is used to determine the wear rate, $w$, from the used input parameters and the depth of the crater:

$$w = \frac{V}{s \cdot F} = \frac{1/3 \cdot \pi h^2 (3R - h)}{\omega R \cdot T \cdot F} \tag{4.16}$$

where $V$ is the crater volume, $s$ is the length of the path travelled by the ball, $F$ is the force against the surface, $h$ is the depth of the crater, $R$ is the ball radius, $\omega$ is the angular velocity of the ball, and $T$ is the wear time. $F$ is adjusted by modifying the distance between the film and the rotating bear, and by changing the holder slope; $\omega$ and $T$ are input in the instrument task; $R$ is a known value, and $h$ is measured by a profilometer after the test.

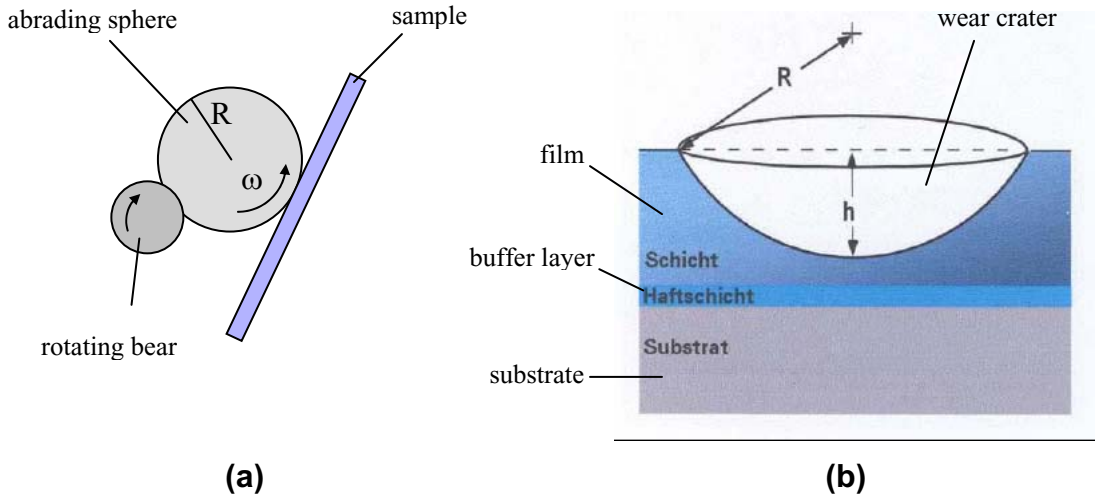


Figure 4.15: (a) Principle of Calo-wear operation and (b) cross-view of the generated crater.

The main advantage of this technique is the reproducibility of the wear results, due to the high precision of the test. Another advantage is that only small sample surfaces are required, since there is only one contact-point between surface and scratching-ball. Measuring the film thickness, $t_c$, is possible, if the ball scratches beyond substrate-film interface:

$$t_c = \frac{xy}{2R} \tag{4.17}$$

where $R$ is the ball radius, and the geometrical parameters x and y of the crater are defined according to figure 4.16.

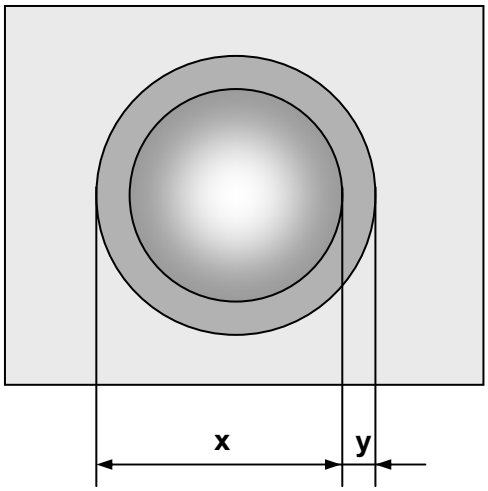


Figure 4.16: Definition of the parameters from a wear crater for thickness determination.

Wear rate measurements were performed by means of a Calotest Compact unit from CSM Instruments, which is installed in the Departament de Física Aplicada i Òptica of the Universitat de Barcelona. The results have been compared to the measurements carried out by a KaloMAX NT instrument, which was developed by BAQ Company in collaboration with the Fraunhofer Society, and is available in the Fraunhofer Institut für Schicht- und Oberflächentechnik (Braunschweig, Germany).